



HAL
open science

Bubble collapse induced cavitation erosion: Plastic strain and energy dissipation investigations

Shrey Joshi, Jean-Pierre Franc, Giovanni Ghigliotti, Marc C. Fivel

► **To cite this version:**

Shrey Joshi, Jean-Pierre Franc, Giovanni Ghigliotti, Marc C. Fivel. Bubble collapse induced cavitation erosion: Plastic strain and energy dissipation investigations. *Journal of the Mechanics and Physics of Solids*, 2020, 134, pp.103749. 10.1016/j.jmps.2019.103749 . hal-02318089

HAL Id: hal-02318089

<https://hal.science/hal-02318089>

Submitted on 5 Dec 2019

HAL is a multi-disciplinary open access archive for the deposit and dissemination of scientific research documents, whether they are published or not. The documents may come from teaching and research institutions in France or abroad, or from public or private research centers.

L'archive ouverte pluridisciplinaire **HAL**, est destinée au dépôt et à la diffusion de documents scientifiques de niveau recherche, publiés ou non, émanant des établissements d'enseignement et de recherche français ou étrangers, des laboratoires publics ou privés.

Bubble collapse induced cavitation erosion: plastic strain and energy dissipation investigations

Shrey Joshi^{1,2}, Jean Pierre Franc², Giovanni Ghigliotti², Marc Fivel¹

¹*Univ. Grenoble Alpes, CNRS, Grenoble INP, SIMaP, 38000 Grenoble, France*

²*Univ. Grenoble Alpes, CNRS, Grenoble INP, LEGI, 38000 Grenoble, France*

A meshless Smoothed Particle Hydrodynamics solver is used to simulate the collapse of a cavitation bubble near a solid material taking into account the complex fluid-structure interaction. A parametric study has been performed to study the effect of stand-off ratio, bubble size, driving pressure and strain rate on the material response. We focus on plastic strain magnitudes and plastic strain energy dissipation to compare different cases and their ability to cause material erosion. Findings indicate that, in the case of repeated collapses, cavities attached to the solid have an ability to initiate damage quicker but exhibit lower erosion rate compared to the cavities detached from the solid. The incubation time does not depend on the size of the bubbles, unlike the erosion rate which is strongly affected by the bubble size. It is also found that the amount of cumulated plasticity is overestimated by more than 150% when the strain-rate sensitivity is not taken into account in the material modelling which suggests that using an appropriate plasticity model that includes strain-rate sensitivity is mandatory while studying the phenomenon of cavitation erosion.

Keywords: Cavitation erosion, Fluid-structure Interaction, plastic strain energy dissipation, strain rate effects, stand-off distance

1. Introduction

To understand the phenomenon of cavitation and its consequence on material erosion has been an important motivation for the numerous research conducted on cavitation [7, 25, 26]. Capturing the complex physics of bubble dynamics during the collapse and measuring accurately the wall pressure still remain a challenge due to the small scale of the phenomenon and the fast dynamics of the process. To assist experimental findings and to better understand the phenomenon, advances have been made in numerical studies of cavitation during the last decades. Most of them have vastly focused on bubble dynamics, to understand the mechanism of the cavitation bubble collapse within the fluid. However, more work is required in order to get a thorough understanding of the material response induced by the collapsing bubbles. For instance, most numerical CFD studies estimate cavitation erosion-prone areas using either peak pressures or Cavitation Aggressiveness Index (CAI) [1-3]. Different CAI have been proposed in the literature, but they are not universal and only valid in specific conditions. Hence there is a need to understand the material response at the fundamental level of a single bubble collapse in order to better predict cavitation erosion damage.

There has been recently a push towards modelling cavitation erosion using Fluid-Structure Interaction solvers [5-6]. A thorough numerical study of cavitation that can provide a holistic understanding, ideally requires a two-way fluid-structure interaction coupling to get realistic results. Earlier studies [5-6] have only used simplified constitutive equations for the material behavior limited to ideally linear isotropic hardening models which cannot capture the non-linear hardening effects. Also, they generally do not consider strain rate hardening effects which can be significant for a phenomenon like cavitation that involves fast dynamics. Past studies have pointed out that, for a material following isotropic hardening, the most probable mechanism of plasticity accumulation for consecutive impact loads is the strain rate effect [7]. In order to gain a better understanding of the mechanisms involved, we developed a cavitation Fluid-Structure Interaction solver capable of solving a single bubble collapse in the fluid and the associated solid response, taking into account both non-linear hardening and strain-rate sensitivity effects in the material.

The SPH FSI solver is developed using an existing 2D open source fluid SPH code SPHYSICS which is used as a basis to develop the solver further [8]. The 2D fluid solver is modified to 2D axisymmetric and the axisymmetric solid solver is

developed in-house. However, axisymmetric SPH solvers suffer from an inconsistent definition of density near the symmetry axis. A new method to mathematically resolve this issue for the axisymmetric solid SPH solver has been published in [9] and will be used in the present study. The axisymmetric fluid and solid solvers were validated against Rayleigh-Plesset collapse and FEM simulations respectively [4, 9]. The two solvers are eventually coupled together to obtain a fully coupled FSI solver capable of solving single bubble collapse over a solid medium to obtain elastic-plastic response using the Johnson-Cook hardening model [10]. Following these developments, this paper presents an application of the SPH FSI solver to a detailed parametric study of the material response for different bubble size, bubble stand-off distance and driving pressure. Results are analyzed in terms of cumulated plastic strain and the effect of the strain rate sensitivity is addressed.

2. Simulation cases and description

In this section, we describe the simulation domain and the parameters used for the simulations. The fluid bubble collapse and the solid response are solved using SPH (more details regarding the methodology are given in [4]). The fluid is treated as weakly compressible and compressibility effects are modeled using Tait's equation of state ,

$$P = B_1 \left[\left(\frac{\rho}{\rho_0} \right)^\gamma - 1 \right] \quad (1)$$

where $\gamma = 7$ and $B_1 = c_0^2 \rho_0 / \gamma$, $\rho_0 = 1000 \text{ kg m}^{-3}$ is the reference density and c_0 is the sound speed at the reference density.

The solid behavior is simulated using the Johnson-Cook model which gives the Yield stress by the following expression,

$$\sigma_y(\varepsilon_p, \dot{\varepsilon}_p) = [A_0 + B_0(\varepsilon_p)^n][1 + C_0 \ln(\dot{\varepsilon}_p^*)] \quad (2)$$

where, A_0 , B_0 , C_0 , n are material constants, $\dot{\varepsilon}_p^* = \frac{\dot{\varepsilon}_p}{\dot{\varepsilon}_{p0}}$ (the non-dimensional effective plastic strain rate) where $\dot{\varepsilon}_{p0}$ is the reference plastic strain-rate of the quasi-static test used to determine the yield stress and hardening parameters A_0 , B_0 and n .

2.1. Simulation domain and cases

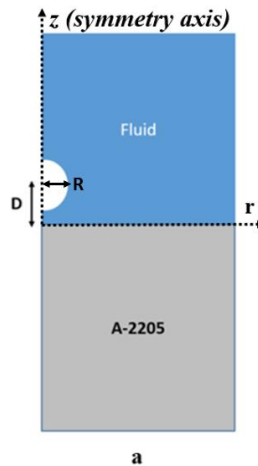


Figure 1. Sketch of the initial simulation domain for axisymmetric SPH FSI simulations.

We simulate the fluid-structure interaction for a single bubble collapse for different bubble sizes, standoff ratios (where the standoff ratio (SR) is defined as $SR=D/R$, D is the distance from the bubble center to the interface and R is the radius of the bubble) and driving pressures in 2D axisymmetric. Figure 1 shows a typical simulation domain for single bubble collapse simulations. The z-axis is the symmetry axis and the r axis is along the fluid-solid interface. The part of the domain above the interface is the fluid where a cavitation bubble is placed and the part of the domain below the interface is the solid which behaves as an elastic-plastic material. It should be noted that the cavitation bubble in the present study is not simulated as a vapour bubble but as a vacuum cavity, this means that the internal pressure of the bubble is 0 at all times during the simulation.

To initiate the collapse, a pressure wave is generated at the top of the fluid domain. The magnitude of the pressure wave can be varied and three different driving pressures were used in the present work (25 MPa, 50 MPa and 75 MPa). The distance D between the bubble center and the interface is varied to produce different cases with varying stand-off ratio ($SR = 1.66, 1.33, 1.0, 0.66 \& 0.33$), where cases with SR less than or equal to 1 correspond to an attached cavity and SR greater than 1 to a detached cavity. In order to vary the bubble size, we keep the number of particles along the bubble radius as a constant $N_{part}=60$ which was found to be an optimum compromise to accurately reproduce the theoretical validations presented in [4]. Hence, increasing the bubble size in the initial configuration is equivalent to increasing the physical distance Δx between two adjacent particles by the same factor. Also the size of the domain scales with the radius of the bubble, e.g. a bubble of twice the radius is simulated using a domain that is scaled by a factor of 2, both in the r and z directions. Since both Δx and the domain size are scaled by the same factor as the bubble radius, the total number of particles in the simulation is kept constant when the bubble size is varied and only changes with the standoff ratio of attached cavities. The total number of particles for the simulations of a detached cavity is 342680 and it can reduce to 320890 in the case of the closest attached cavity ($SR=0.33$). We use three different bubble sizes (0.1 mm, 0.15 mm & 0.2 mm) to run a parametric study on the effect of bubble size on the material response.

2.2. Fluid and material parameters

The fluid and material parameters for the present simulations have been listed in table 1.

Table 1. Table showing parameters for the fluid and solid used in the FSI simulations.

Parameter	Fluid (Water)	Solid (A-2205)
Density (kg/m^3)	1000	7800
Sound speed (m/s)	1500	4883.33
α (artificial viscosity)	1	1
β (artificial viscosity)	2	2
Young's Modulus	-	186 GPa
Poisson ratio	-	0.3
A_0 (in equation 2)	-	508 MPa
B_0 (in equation 2)	-	832 MPa
C_0 (in equation 2)	-	0.031

2.3. Estimation of incubation time and erosion rate

Although this study only presents results for a single bubble collapse, some qualitative results can be deduced for the case of repeated bubble collapses. In order to do so we consider two important quantities related to material erosion: incubation time (marked as A in figure 5) and erosion rate. Figure 5 shows a typical mass loss curve for a material exposed to cavitation. Incubation time is the exposure time required by the material to initiate surface erosion and indicates how quickly a material

exposed to cavitation will start to erode. On the other hand, erosion rate would indicate the rate of material removal after the incubation period. These two quantities put together are considered to provide a good measure of the erosion characteristics under repeated cavitation loads.

Let us consider that the energy dissipated by the material after a single impact is E . It can reasonably be expected that the absorbed energy after n impacts is of the order of $n.E$. The volume loss (V_L) can then be approximated by $V_L = n.E/K$ (where K is the material fracture toughness, which indicates the amount of energy absorbed per unit volume until fracture). Therefore, the erosion rate (E_R i.e. volume loss per impact) is $E_R = V_L/n = E/K$. Since the material toughness (K) is a constant for a given material, the energy absorbed by the material after a single impact can be considered as an indicator of the erosion rate for multiple impacts. The higher the absorbed energy, the higher the erosion rate.

For incubation time estimation, let us consider V , the volume of the plastic deformed zone for a single impact. Lets assume that the plastic zone size still remains of the order of V for each subsequent impact. It could then be assumed that the incubation time corresponds roughly to the critical number of impacts n_c required to reach the fracture toughness in that volume V . The energy absorbed by the material would then be $V.K$. Since it is also $n_c.E$, we have $V.K = n_c.E$ so that the incubation time (or more precisely the critical number of impacts at failure) would be $n_c = K/(E/V)$. This suggests that the incubation time n_c should vary as the inverse of the absorbed energy density E/V . Hence, the higher the absorbed energy density, the lower the incubation time.

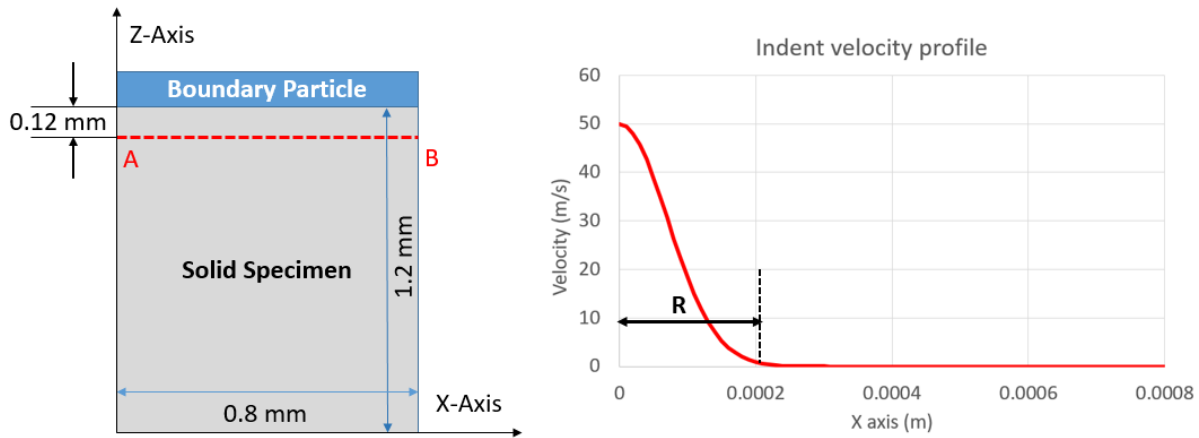


Figure 2. The figure on the left shows the computational domain for solid simulation, the boundary particles marked in blue are given a downward velocity with a Gaussian shape as plotted on the right. The extent of the velocity profile R is defined as the distance from the center where the velocity is 1% of the peak value, a non-uniform but constant velocity is given to the indenter.

In order to validate the above stated hypothesis, we use a simplified case of mass loss simulations. Figure 2 shows the simulation domain where a solid specimen is indented using boundary particles on the top of the domain (as shown in Figure 2 left). The graph on the right shows the velocity of boundary particles in the downwards direction which creates an indentation into the solid specimen. The material follows the Johnson-Cook model for elastic visco-plastic behavior and the material damage is simulated using a simplified damage criterion based on the rupture strain [23, 24]. A critical value of rupture strain, ϵ_u , is defined to predict whether the SPH particle is damaged or not. In the following simulations, we will choose $\epsilon_u=0.03$. For a given particle, if the cumulated plastic strain exceeds ϵ_u , the particle is assumed damaged and it does not contribute anymore to the nearby particle interactions. The objective of the simulations is to obtain the mass loss curves for different radii of the indentation profile marked as R in fig 2 right (0.1, 0.141, 0.2 & 0.283 mm) and also to calculate the total absorbed energy and absorbed energy densities. In order to calculate the total absorbed energy, the area under the stress strain curve for each particle is calculated and then multiplied by the volume occupied by that particle to obtain energy absorbed by each particle. This quantity is summed up for all particles to obtain the total energy dissipated by the solid. To obtain the dissipated energy density, the total dissipated energy is divided by the volume of the plastic strain zone. The volume of the plastic strain zone is obtained by adding the volume occupied by each particle that has undergone plastic

deformation. Finally, the erosion rate is computed from the total mass of the damaged particles per unit of time. Figure 3 and Figure 4 plot the total dissipated energy vs the erosion rate and the dissipated energy density vs the incubation time respectively. These quantities were obtained from the indenter mass loss simulations for four different radii. The trend clearly shows that the total dissipated energy increases linearly with the erosion rate and the dissipated energy density decreases linearly with the incubation time, thus validating the hypothesis. In the next section, we will use these quantities to derive the incubation time and the erosion rate in the case of bubble collapses.

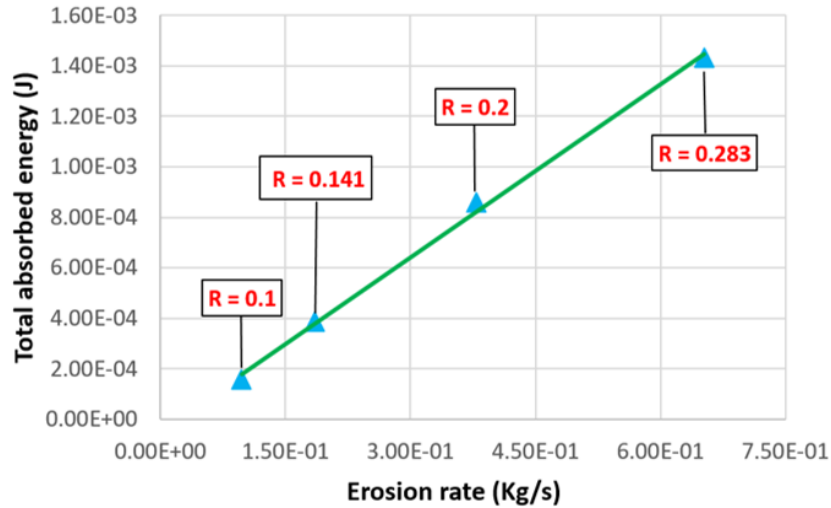


Figure 3. Total dissipated energy vs erosion rate for 4 different indenter radius ($R = 0.1, 0.141, 0.2$ & 0.283 mm).

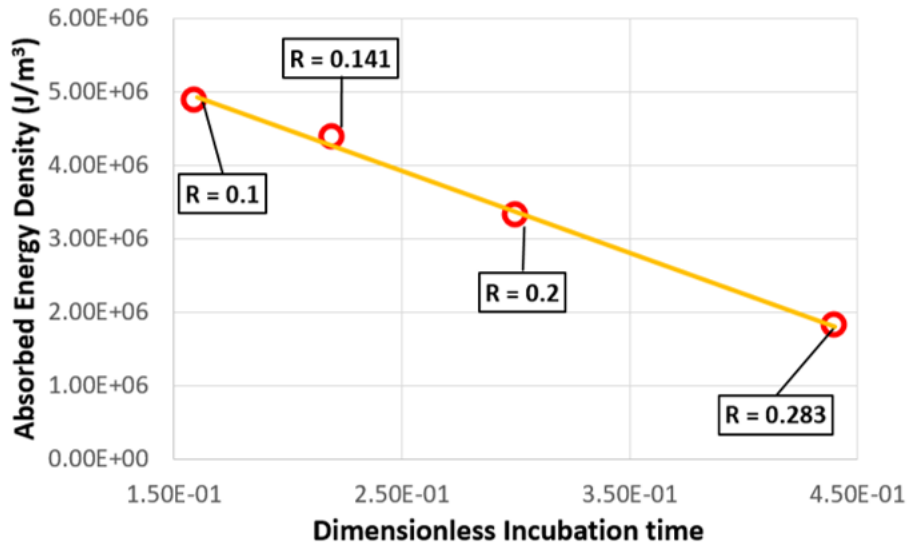


Figure 4. Dissipated energy density vs dimensionless incubation time, where the dimensionless incubation time is defined as the ratio of the incubation time by the total simulation time. The total simulation time is kept constant at $1.5 \mu\text{m}$ for all 4 simulations with different indenter radius ($R = 0.1, 0.141, 0.2$ & 0.283 mm).

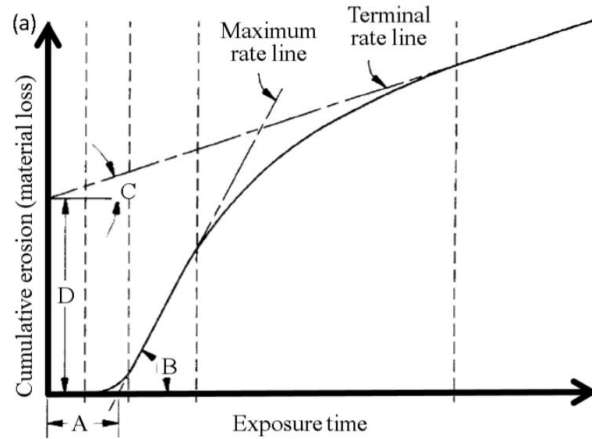


Figure 5. Characteristics of typical cumulative erosion versus exposure time curve. A = nominal incubation time; (B) = maximum erosion rate; (C) = terminal erosion rate; and D = terminal line intercept [18].

3. Results and discussions

3.1. Effect of stand-off ratio

To understand the effect of the stand-off ratio on the mass loss curve resulting from a bubble collapse, we vary SR while keeping the bubble size at $R=0.15$ mm and the driving pressure constant at 50 MPa. The material responses obtained for seven different stand-off ratios are presented in this section: SR = 1.66, 1.5, 1.33, 1.2, 1.0, 0.66 & 0.33. A stand-off ratio of more than 1 corresponds to a detached cavity (when the bubble surface does not touch the solid) and a stand-off ratio less than or equal to 1 corresponds to an attached cavity (when the bubble surface touches the solid). Figure 6 shows contours of the plastic strain in the material for all the seven cases, figure 6d-g shows plastic strain contours for detached cavities (SR = 1.2, 1.33, 1.5 & 1.66 respectively) and figure 6 a-c are magnified contours (magnified over the white dashed rectangle shown in figure 6g) for attached cavities (SR = 0.33, 0.66 & 1.0 respectively). The reason why the contours for attached cavities are magnified is because the attached cavity produces a very tiny zone of plastic deformation compared to the detached cavities which would not be clearly noticeable in a non-magnified contour.

Attached cavities produce two distinct zones of plastic deformation: a primary plastic deformation zone very close to the symmetry axis and a secondary plastic deformation zone away from the symmetry axis. A detailed description of the plasticity mechanism in the case of an attached cavity was presented in an earlier study [4]. It was shown that the primary plastic deformation zone is initiated by the micro-jet hitting the solid and later increased when the shock wave emitted by the toroid bubble collapse reaches the symmetry axis. The secondary plastic deformation zone is only due to the shock wave generated by the toroid collapse. It can be clearly observed from Figure 6a-c that for attached cavities the highest maximum plastic strain is obtained for SR = 1.0. This corresponds to the case where the micro-jet from the bubble surface gain the highest speed at the time of interaction with the solid surface. This highest kinematic energy in the jet leads to the highest pressure on the solid. However, while comparing SR = 0.66 and SR = 0.33, it would be expected that SR = 0.66 should produce higher maximum plastic strain as it would have a higher micro-jet velocity, but an opposite trend is observed. The trend reverses because the plastic strain at the center is not just due to the micro-jet but also to the shock wave from the toroid collapse. From the secondary plastic strain zone, it can be observed that the toroid collapse point for SR = 0.33 is closer to the center compared to SR = 0.66. Hence the shock wave emitted from the toroid collapse produces a higher plastic strain at the center for SR = 0.33 compared to SR = 0.66. So even though the micro-jet should produce a higher plastic strain at the center for SR = 0.66, the higher additional plastic strain due to the toroid collapse supersedes the effect, leading to a higher plastic strain in the material for SR = 0.33.

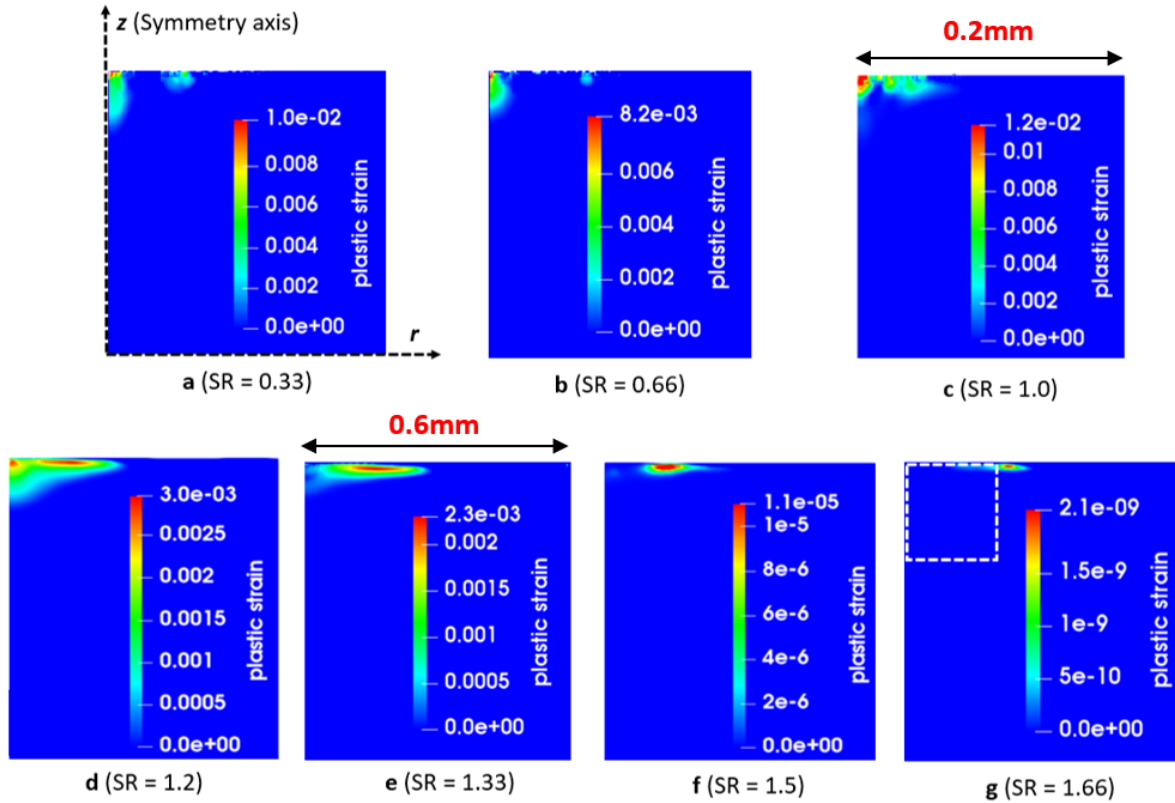


Figure 6. Plastic strain contours for different stand-off ratios (for a 0.15 mm bubble radius and 50 MPa driving pressure) (a) for $SR = 0.33$, (b) for $SR = 0.66$, (c) for $SR = 1.0$, (d) for $SR = 1.2$, (e) for $SR = 1.33$, (f) for $SR = 1.5$, (g) for $SR = 1.66$ (the contours in figure 6a, 6b & 6c are magnified on the white dashed rectangle in figure 6g).

For a detached cavity (Figure 6d-g), the plastic strain is only due to the shock wave impact. It is obvious that the higher the stand-off ratio, the lower the shock wave pressure becomes by the time it reaches the interface, hence producing lower plastic deformation. This is clearly evidenced in Figures 6d-g by the maximum plastic strain amplitude computed for $SR = 1.2, 1.33, 1.5$ & 1.66 , where the lower the stand-off ratio, the higher the maximum plastic strain amplitude. Note that for the detached cavity simulations, the maximum plastic strain does not occur at the symmetry axis but at an offset from the symmetry axis especially for higher stand-off ratios ($SR = 1.33, 1.5$ & 1.6). Previous study has dealt with this phenomenon in detail for the case $SR=1.33$ [4] and shown that this is due to the geometry of the spherical shock wave intersecting with a flat surface. When the shock wave travels along the interface, its velocity decreases as it moves further from the symmetry axis. Near the symmetry axis, the velocity of the shock wave is high and consequently the rate of loading is high. This does not allow the material to respond to the load due of its inertia, thus leading to a lower plastic strain close to the symmetry axis even though the maximum pressure acts at the symmetry axis.

However, it can be noted that for $SR = 1.2$, there is a tiny zone of relatively high plastic deformation close to the symmetry axis. This is because the material deformation can happen due to two reasons: either by the shock wave impinging on material surface or by the impulse momentum of the liquid micro jet impinging first on the bubble surface and then on the material surface. For cavities far from the material surface ($SR = 1.33$ and above), the impulse momentum of the micro-jet is mostly converted in shock wave energy when it reaches the material surface. However, for $SR = 1.2$, where the distance between the solid surface and the bubble surface is smaller, the solid surface experiences both the shock wave (that causes some plastic strain at an offset from the symmetry axis as visible in Figure 6d) and an impulse momentum created by the liquid micro-jet (that causes the plastic strain very close the symmetry axis also visible in Figure 6d).

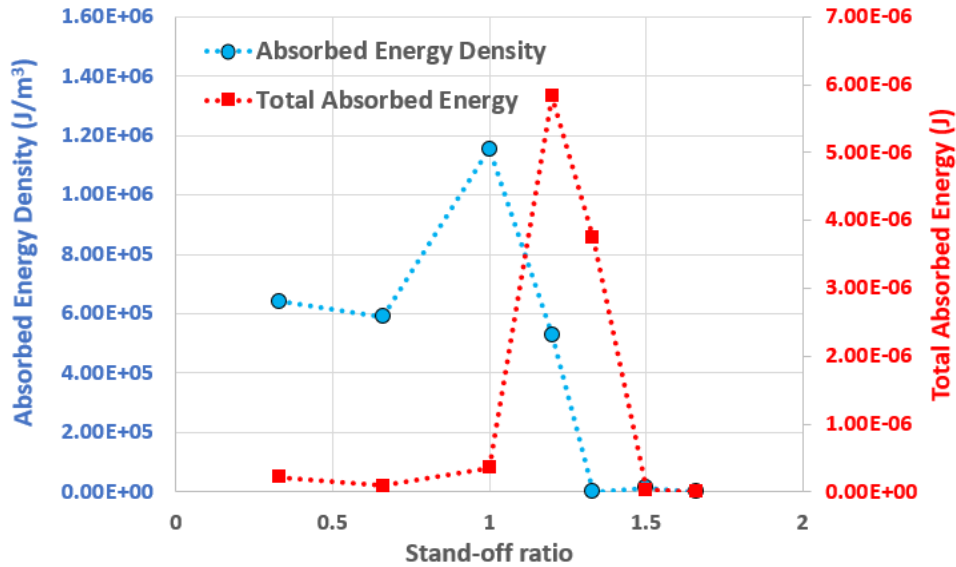


Figure 7. Evolution of the dissipated energy density and the total dissipated energy wrt the stand-off ratio for FSI single bubble collapse simulations (bubble radius and driving pressure are kept at 0.15 mm and 50 MPa respectively).

The above results show a clear difference in the plastic deformation mechanism for attached and detached cavities. We observe that the maximum plastic strain in the case of an attached cavity is generally much higher compared to a detached cavity but the volume of the plastically deformed zone for a detached cavity is much higher than for an attached cavity, which makes it difficult to predict the erosion ability of bubble collapses with different stand-off ratio.

In order to estimate the erosion ability of the different cases presented in this section, we now focus on the two quantities defined earlier: the dissipated energy density (possible indicator of the incubation time) and the total dissipated energy (possible indicator of the erosion rate). They are both plotted in Figure 7 for the seven stand-off ratios. For attached cavities ($SR \leq 1$), it can be observed that the dissipated energy density is higher compared to detached cavities, which suggests a smaller incubation time and possibly a quicker initiation of erosion. Within the attached cavities, for different stand-off ratios, the maximum dissipated energy density is observed for a stand-off ratio of 1.0 which should lead to the fastest incubation during repeated impacts.

However due to the large volume of the plastic zone for detached cavities closest to the solid ($SR = 1.2$ & 1.33), the total absorbed energy which is an indicator for the erosion rate is much higher compared to attached cavities. Hence, even though the incubation time for $SR = 1.2$ & 1.33 is lower than for attached cavities, the results suggest that thereafter the erosion rate could be a magnitude higher for detached cavities close to the solid compared to attached cavities. For detached cavities farther away from the wall ($SR \geq 1.5$), the pressure of the shock wave decreases by the time it reaches the interface and could not produce high plastic strain.

3.2. Effect of driving pressure

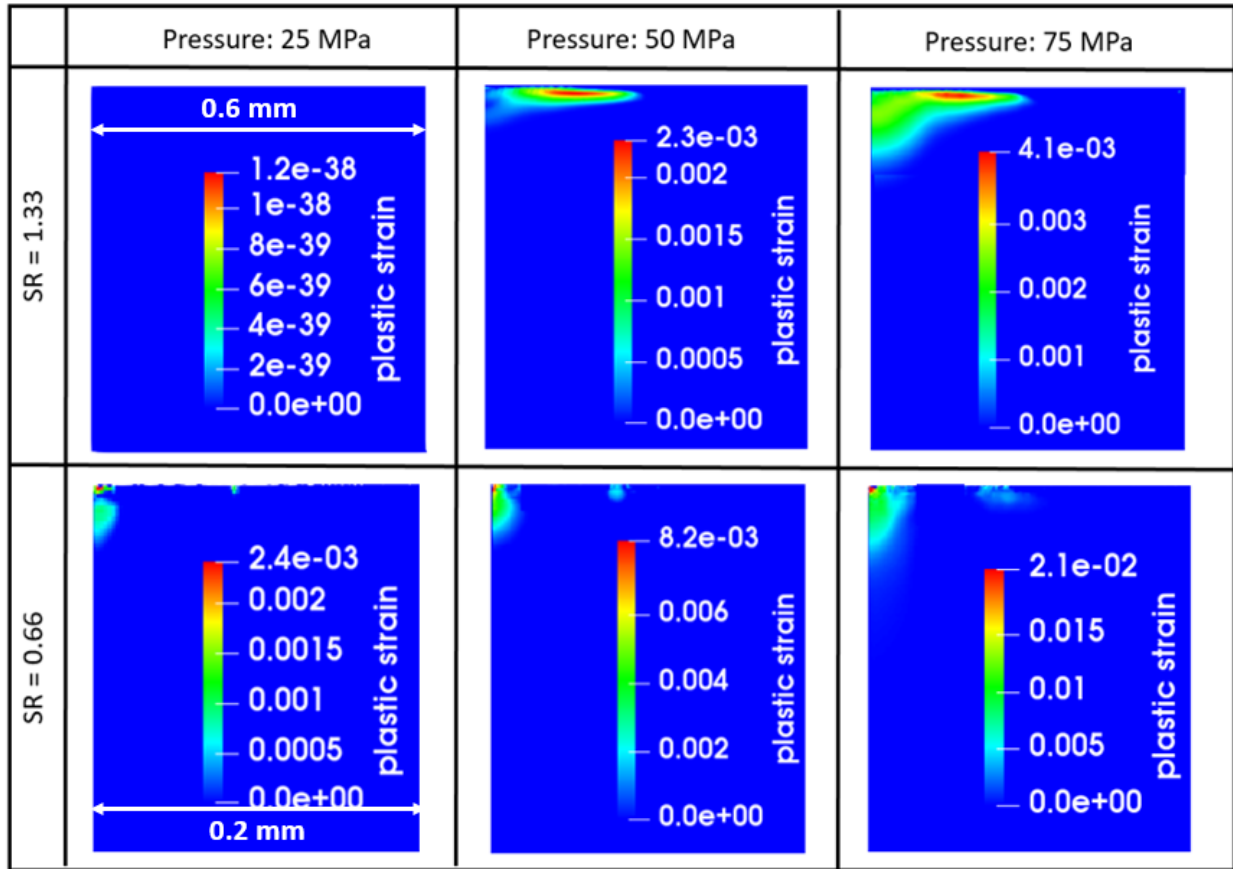


Figure 8. Contours of plastic strain for 3 different driving pressure (25 MPa, 50 MPa & 75 MPa) for detached cavity (SR = 1.33) and attached cavity (SR = 0.66) while keeping the bubble radius constant at 0.15 mm. All attached cavity contours (on the lower row) are magnified contours over the white dashed rectangle in Figure 6g.

We present results for 3 different driving pressures (25 MPa, 50 MPa & 75 MPa) for an attached cavity (SR = 0.66) and a detached cavity (SR = 1.33), keeping the bubble radius constant at 0.15 mm. Contour plots of the plastic strain amplitude reached at the end of the simulation for the 6 cases are presented in Figure 8. For detached as well as attached cavities, the maximum plastic strain increases with increase in driving pressure, which is expected as a higher pressure can produce a higher micro jet velocity leading to higher pressure on the solid.

Figure 9 shows the evolution of the dissipated energy density and the total dissipated energy for both attached and detached cavities plotted against the driving pressure. It can be clearly observed that a higher driving pressure leads to a higher dissipated energy density and therefore a higher total dissipated energy. The dissipated energy density is higher for attached cavity for all driving pressures compared to detached cavity. However, the higher volume of the plastic zone in the case of a detached cavity leads to a higher total dissipated energy compared to an attached cavity. The difference in total dissipated energy and hence erosion rate for detached and attached cavity seems to be more prominent as the driving pressure increases.

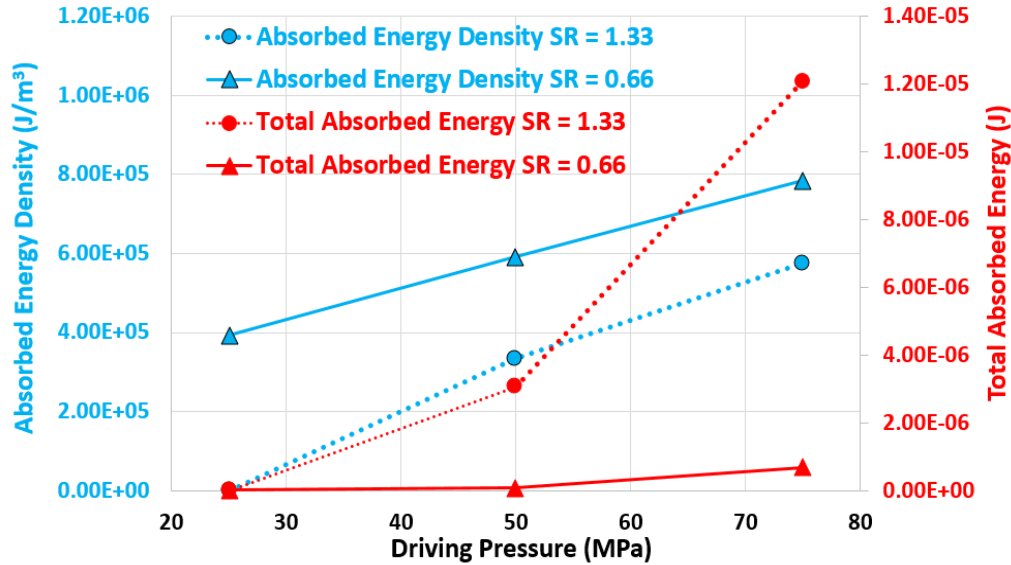


Figure 9. Plot of absorbed energy density and total absorbed energy wrt driving pressure for 2 different stand-off ratio (SR = 0.66 & 1.33) for FSI single bubble collapse simulations.

3.3. Effect of bubble size

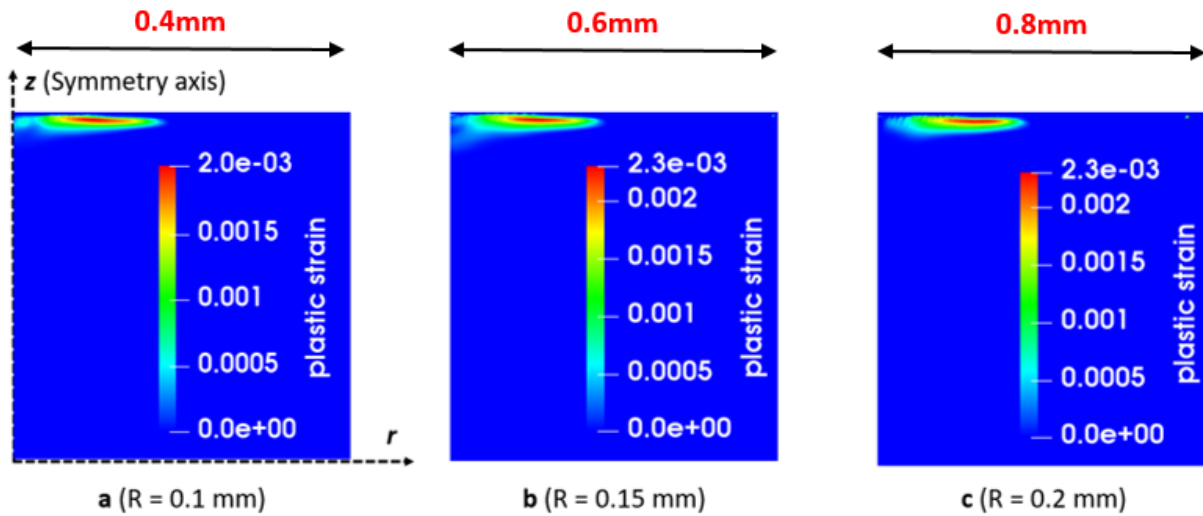


Figure 10. Contours of plastic strain for 3 different bubble radius ($R = 0.1$ mm, 0.15 mm & 0.2 mm) for a detached cavity (SR = 1.33) while keeping driving pressure constant at 50 MPa.

To understand the effect of the bubble size, we use three different bubble radii ($R = 0.1$ mm, 0.15 mm & 0.2 mm) for the case of a detached cavity (SR = 1.33) while keeping driving pressure constant at 50 MPa. The contours of the plastic strain suggest that the maximum plastic strain remains almost the same for different bubble radius. This is because the micro-jet velocity is independent of the bubble size and hence the shock wave pressure at the interface remains almost the same for all the bubble radii.

It could also be observed that the plastic strain close to the symmetry axis decreases as the bubble radius increases. This behavior can be attributed to the speed of the shock wave traveling along the interface. When the point of collapse is closer to the interface, the wave velocity along the interface near the symmetry axis is smaller and the plasticity is higher because of the inertial effects [4]. For a given stand-off ratio, the lower bubble size leads to a lower axial distance between the

collapse point and the interface and hence a lower shock wave velocity along the interface near the symmetry axis. Thus, the material has more time to react to the load which translates into plastic deformation.

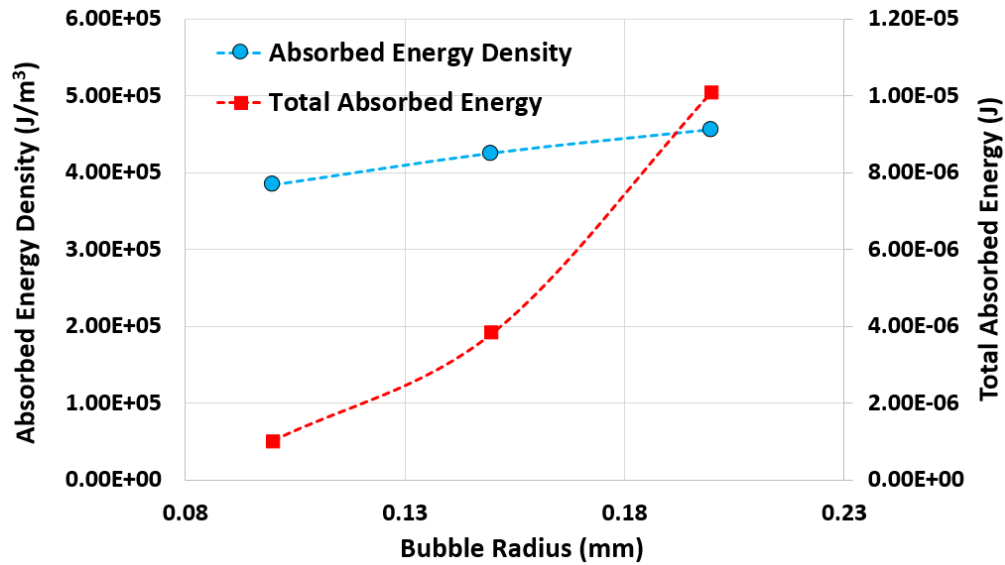


Figure 11. Dissipated energy density and total dissipated energy wrt the bubble radius (for $SR = 1.33$ and driving pressure of 50 MPa) for FSI cavitation collapse simulations.

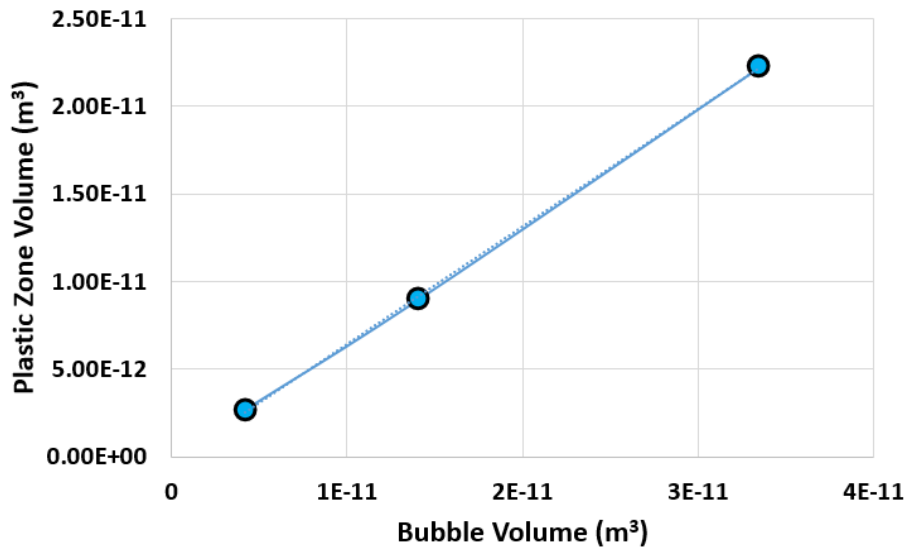


Figure 12. Plot of plastic zone volume vs bubble volume for three bubble radius (0.1, 0.15 & 0.2 mm), $SR = 1.33$ and driving pressure of 50 MPa for FSI single bubble collapse simulations.

As mentioned in section 2.1, the domain size scales with the bubble radius. Hence, the dimensions of the contours shown in Figure 10 also scale with the bubble radius and therefore the volume of the plastic strain zone increases with increasing bubble radius. Thus, even though the dissipated energy density exhibits almost similar values for all bubble radii, the total dissipated energy increases significantly with increasing bubble radius. This suggests that the incubation time for all bubble radii should be almost the same whereas the erosion rate should increase significantly with increasing radius.

To understand the relationship between the bubble volume and the plastic zone volume, we plot in Figure 12 the plastic zone volume on the left axis and the volume of the bubble for three bubble radius (0.1, 0.15 & 0.2 mm) while keeping the

standoff ratio at $SR=1.33$ and the driving pressure at 50 MPa. It can be observed from Figure 12 that as the bubble volume increases the plastic zone volume increases linearly. In section 3.5, we will address this relationship by introducing the potential energy of the bubble.

3.4. Effect of strain rate

The effect of strain rate can be demonstrated by switching off the strain rate terms in equation 2 by substituting C as 0 instead of 0.031. We present results for $C = 0$ and $C = 0.031$ for three stand-off ratios ($SR = 0.33, 1.0$ & 1.33), keeping the bubble radius and driving pressure constant at 0.15 mm and 50 MPa respectively. The two contours in column **a** of Figure 13 are obtained for a detached cavity ($SR = 1.33$). It is observed that the strain rate insensitive case produces a 60% higher maximum plastic strain and a 40% higher volume of the plastically deformed zone. Also, for the attached cavity case shown in column **b** ($SR = 1.0$) and **c** ($SR = 0.33$), the plastic strain is almost 180% and 220% more in the strain rate insensitive case compared to the strain rate sensitive case for column **b** and **c** respectively. Hence the strain rate sensitivity has an even more prominent effect on the plastic strain developed for attached cavities. The case presented in column **c** ($SR = 0.33$) shows an interesting effect. The primary and secondary plastic deformation zones (section 3.1 gives description about these zones) show a similar magnitude of the plastic strain for the strain rate insensitive case. However, the strain rate sensitive case shows a higher magnitude of plastic strain in the primary plasticity zone compared to the secondary plasticity zone.

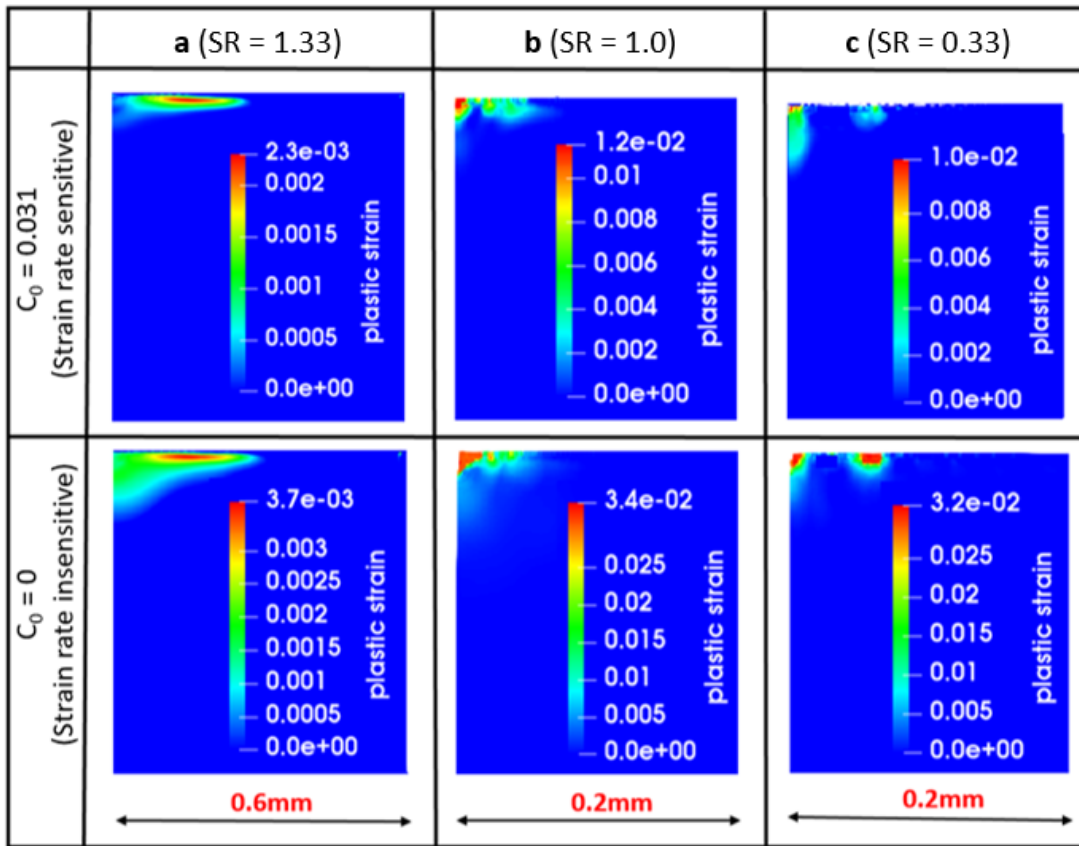


Figure 13. Contours of plastic strain for 3 different stand-off ratio ($SR = 1.33, 1.0$ & 0.33) showing both strain rate sensitive ($C = 0.031$) and insensitive ($C = 0$) response while keeping the bubble radius and driving pressure constant at 0.15 mm and 50 MPa respectively. Column **a** shows results for $SR = 1.33$, column **b** shows results for $SR = 1.0$ and column **c** shows results for $SR = 0.33$; All attached cavity contours (column **b** and **c**) are magnified contours over the white dashed rectangle in figure 6g.

3.5. Plastic deformation potential

This section compares the plastic energy dissipated by the material to the potential energy of the bubble, which gives a relative potential of the cavity to produce plastic deformation in the material. We consider the ratio of the two quantities: dissipated plastic energy ($E_{Plastic}$) and bubble potential energy ($E_{Potential}$ which is given by the driving pressure multiplied by the initial volume of the cavity). The ratio is hereafter in the article referred to as *Plastic Deformation Potential* (PDP) given by the following,

$$\% PDP = \frac{E_{Plastic}}{E_{Potential}} \times 100 \quad (2)$$

The %PDP is plotted in Figure 14 against the stand-off ratio for 7 cases (SR = 0.33, 0.66, 1.0, 1.2, 1.33, 1.5 & 1.66) for the same driving pressure (50 MPa) and same bubble radius (R=0.15mm) and consequently for the same bubble potential energy. It can be observed that the amount of plastic energy absorbed by the material as a percentage of the initial bubble potential energy (%PDP) for attached cavities lies within a range of 0.09-0.019% (SR = 0.33, 0.66 & 1). However, the %PDP is around 0.53-0.83% for detached cavities close to the solid (SR = 1.2 & 1.33), which is more than a magnitude higher than the attached cavities. Furthermore, as the stand-off ratio increases for detached cavities (SR = 1.5 & 1.66), the bubble potential energy that translates into plastic energy goes down by a few orders of magnitude. Hence the *plastic deformation potential* of a cavity detached from the solid but placed close enough to the solid seems to be the highest compared to either an attached cavity or a detached cavity with higher stand-off (SR>1.33).

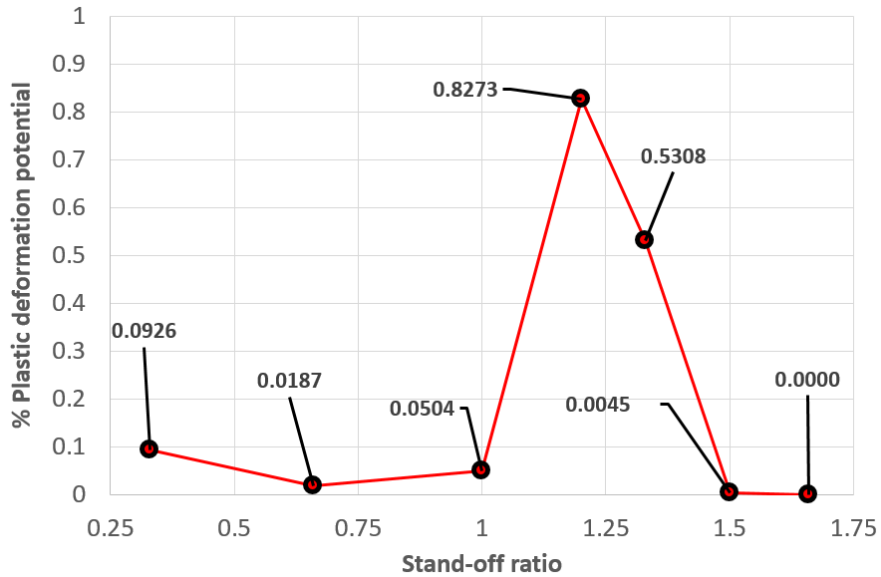


Figure 14. Plot of %PDP vs stand-off ratio (for bubble radius of 0.15 mm and driving pressure of 50 MPa) for FSI single bubble collapse simulations.

4. Conclusions and future work

Fluid-structure Interaction simulations of single bubble collapse for different stand-off ratio, driving pressure and bubble radius has been presented in the article. Results reveal that for varying stand-off ratio while keeping the bubble radius and driving pressure constant, the attached cavities ($SR \leq 1$) show a higher plastic strain magnitude and a higher absorbed energy density which suggests a smaller incubation time in the case of repeated impacts. However, the volume of the plastic deformation zone and the total dissipated energy are much larger for detached cavities so that the erosion rate should be much higher in the case of repeated impacts.

The results show that, as expected, both the dissipated energy density (hence the incubation time) and the total dissipated energy (hence the erosion rate) increase with increasing the driving pressure. The change in bubble radius while keeping other parameters constant do not affect the magnitude of the plastic strain and the dissipated energy density much, which suggests that irrespective of the size of the cavitation bubble, the incubation time should remain similar for all bubble sizes.

However, since the volume of plastically deformed zone goes linearly with the bubble volume, the total dissipated energy increases significantly with increasing the bubble size, which suggests that the erosion rate also increases significantly for repeated collapses.

Fluid-Structure Interaction studies in the past have not considered strain rate sensitivity while defining the plasticity model of the solid material [5-6]. The strain rate effects presented in the paper demonstrate that the magnitude of the plastic strain is over predicted while using plasticity models that do not include strain rate sensitivity. The over prediction of the magnitude of plastic strain is around 60% for detached cavities and around 200% for attached cavities. It can be concluded that neglecting strain rate effects in the constitutive model of the solid material leads to an under prediction of incubation time and an over prediction of the erosion rate.

A quantity called *plastic deformation potential* (PDP) is introduced in the article which refers to the plastic energy absorbed by the material divided by the initial potential energy of the cavity. PDP indicates the relative efficiency of a cavity to translate its potential energy into plastic energy. It is observed that detached cavities close to the solid wall can produce the highest PDP of the order of 0.83% (only 0.83% of bubble potential energy translates to plastic energy), the next most efficient are the attached cavities that can produce PDP of the order of 0.05% and the detached cavity far from the solid ($SR > 1.5$) produce extremely low PDP values. These results can be directly used in CFD calculations to better estimate the area prone to cavitation erosion.

A novel approach has been proposed where single impact FSI calculations are used to estimate both mass loss and incubation time. Hence in an initial model using this approach, it is assumed that the order of energy absorbed at each subsequent collapse remain the same as E and the order of volume of the plastic deformation zone remain V . In future, consecutive bubble collapse simulation will be conducted in a similar parametric study as presented in this paper. The consecutive collapse simulations will be used to re-validate the assumption used in this model and make modifications if deemed necessary.

Acknowledgement

This project has received funding from the European Union's Horizon 2020 research and innovation program under the Marie Skłodowska-Curie grant agreement No 642536.

References

- [1] P. K. Koukouvini, G. Bergeles, M. Gavaise, "A cavitation aggressiveness index within the Reynolds averaged Navier Stokes methodology for cavitating flows," 2015, Journal of Hydrodynamics, Elsevier, 27(4)579-586, DOI: 10.1016/S1001-6058(15)60519-4
- [2] Z. R. Li, "Assessment of cavitation erosion with a multiphase Reynolds-Averaged Navier-Stokes method," PhD Thesis, TU Delft, 2012
- [3] Y. C. Wang and C. E. Brennen, "Numerical Computation of Shock Waves in a Spherical Cloud of Cavitation Bubbles," Journal of Fluids Engineering, vol. 121, pp. 872-880, 1999
- [4] S. Joshi, J.P. Franc, G. Ghiglotti, M. Fivel, 'SPH modelling of cavitation bubble collapse near an elasto-visco-plastic material', Journal of Mechanics and Physics of Solid, Volume 125, April 2019, Pages 420-439, December 2018, <https://doi.org/10.1016/j.jmps.2018.12.016>
- [5] C-T Hsiao A. Jayaprakash, A. Kapahi, J.-K. Choi and G. L. Chahine, "Modelling of material pitting from cavitation bubble collapse," Journal of Fluids Mechanics, 2014, vol. 755, pp. 142-175.
- [6] C. K. Turangan, G. J. Ball, A. R. Jamaluddin, T. G. Leighton, "Numerical studies of cavitation erosion on an elastic-plastic material caused by shock-induced bubble collapse," Proceedings of the Royal Society A, 2017, vol. 473

- [7] M. Fivel, J. -P. Franc, S. C. Roy, "Towards numerical prediction of cavitation erosion," *Interface Focus*, 5, 20150013. <http://dx.doi.org/10.1098/rsfs.2015.0013>
- [8] M. Gómez-Gesteira, B.D. Rogers, R.A. Dalrymple, A.J.C. Crespo, and M. Narayanaswamy, 2010, User Guide for the SPHysics Code v2.0. <http://wiki.manchester.ac.uk/sphysics>
- [9] S. Joshi, J.P. Franc, G. Ghiglotti, M. Fivel, An axisymmetric Solid SPH solver with consistent treatment of particles close to the symmetry axis: Application to cavitation erosion, submitted to *Journal of Computational Particle Mechanics*
- [10] G.R. Johnson, W.H. Cook, Fracture characteristics of three metals subjected to various strains, strain rates, temperature and pressure, *Engineering Fracture Mechanics*, Vol. 21, No. 1, pp. 31-48, 1985.
- [11] L. Brookshaw, "Smooth particle hydrodynamics in cylindrical coordinates", 2003, *ANZIAM J*, 44, C114
- [12] J. J. Monaghan, "Smoothed Particle Hydrodynamics", 2005, *Rep. Prog. Phys.*, 68, 1703-1759
- [13] M. Omang, S. Borve, J. Trulsen, "SPH in spherical and cylindrical coordinates" 2006, *Journal of Computational Physics*, vol. 213, pages 391-412
- [14] M. Omang, S. Borve, J. Trulsen, "Shock collisions in 3D using an axisymmetric regularized smoothed particle hydrodynamics code", 2007, *Shock Waves*, vol. 16, pages 467-475
- [15] D. García-Senz, A. Relaño, R. M. Cabezón, E. Bravo, Axisymmetric smoothed particle hydrodynamics with self-gravity, *Monthly Notices of the Royal Astronomical Society*, Volume 392, Issue 1, 1 January 2009, Pages 346–360, 2008, <https://doi.org/10.1111/j.1365-2966.2008.14058.x>
- [16] J.J. Monaghan, H. Pongracic, Artificial viscosity for particle methods, Volume 1, Issue 3, May 1985, Pages 187-194, *Applied Numerical Mathematics*, [https://doi.org/10.1016/0168-9274\(85\)90015-7](https://doi.org/10.1016/0168-9274(85)90015-7)
- [17] J. J. Monaghan, On the problem of penetration in particle methods, 1989, *Journal Computational Physics*, 82: 1-15.
- [18] S.C. Roy, "Modeling and analysis of material behavior during cavitation erosion" PhD Thesis, University Grenoble Alpes, 2015.
- [19] Z. Li, M. Pourquie and T.V. Terwisga, Assessment of Cavitation Erosion with a URANS Method, *Journal of Fluids Engineering* 136(4):041101 · April 2014
- [20] C. Leclercq, A. Archer, R. Fortes-Patella and F. Cerru (2017). Numerical Cavitation Intensity on a Hydrofoil for 3D Homogeneous Unsteady Viscous Flows. *International Journal of Fluid Machinery and Systems*. 10(3), pp. 254-263.
- [21] S. Schenke & T v Terwisga, Erosive Aggressiveness of Collapsing Cavitating Structures, The 10th International Symposium on Cavitation (CAV2018), May 14 – 16, 2018, Baltimore, Maryland, USA
- [22] R. Fortes Patella, G. Challier, J-L Reboud, A. Archer. Energy Balance in Cavitation Erosion: From Bubble Collapse to Indentation of Material Surface. *Journal of Fluids Engineering*, American Society of Mechanical Engineers, 2013, 135 (1), DOI: 10.1115/1.4023076
- [23] S.C. Roy, J.-P. Franc, C. Pellone, M. Fivel, Determination of cavitation load spectra – Part 1: Static finite element approach, *Wear* (2015). doi:10.1016/j.wear.2015.09.006.
- [24] S.C. Roy, J.-P. Franc, N. Ranc, M. Fivel, Determination of cavitation load spectra—Part 2: Dynamic finite element approach, *Wear* (2015). doi:10.1016/j.wear.2015.09.005.
- [25] M. Fivel, J.P. Franc , *ASM Handbook*, Volume 18, Friction, Lubrication, and Wear Technology, pp.290-301, (2017).

[26] J-P. Franc and J-M. Michel, (2006). Fundamentals of cavitation. Kluwer Academic Publisher.*